ON SUN TESTING OF A SINGLE SPIKE OF THE SPIKY CENTRAL RECEIVER AIR PRE-HEATER (SCRAP)

J.E. Hoffmann[1], R.J. Janse van Vuuren[2], B. Sebitosi[3]

[1] Solar Thermal Energy Research Group (STERG), Stellenbosch University, hoffmaj@sun.ac.za

[2] STERG, Stellenbosch University, Private Bag X1, Matieland 7602, South Africa; E-Mail: rjvvuuren@gmail.com

[3] STERG, Stellenbosch University, sebitosi@sun.ac.za

Abstract: The Spiky Central Receiver Air Pre-heater (SCRAP) is the pressurized air central receiver concept envisaged for implementation in an asynchronous combined Brayton-Rankine cycle. The receiver would need to provide outlet air temperatures above 800 ˚C with a sub-30 kPa pressure drop to ensure efficient power generation when thermal energy storage is implemented. This study develops an experimental receiver, approximating a full-scale receiver, to investigate the thermal characteristics associated with a single spike of the SCRAP in on-sun conditions.

The receiver achieved thermal efficiencies of up to 84% at high air flow rates, however, these efficiencies were only obtained at low wind speeds, as the receiver also proved to be susceptible to convective losses. Heat transfer enhancements in the form of helically coiled fins at the front half of the spike improved the thermal efficiency by 8% at low flow rates, with little benefit at high flow rates. As the spike irradiation exposure increases exponentially towards the root, full- length finned spikes with optimized internal geometries are expected to offer higher efficiencies at low flow rates. Measures to reduce convective losses and mitigate high temperatures at critical structural areas were suggested. Cost effective full-scale manufacturability and practicality remains a concern which needs to be addressed.

Keywords: SCRAP, CSP, pressurized air receiver.

1. Introduction

Concentrating solar power (CSP) is largely centered around solar tower and Parabolic trough (PT) technologies. While PT power has long dominated the CSP market, a recent shift in technology has brought attention to solar tower receivers for their ability to produce concentration ratios of up to 1000, as opposed to a typical concentration ratios of 30-80 for PTs. The higher temperatures provided by solar towers facilitate the integration of more efficient power cycles, reducing generation costs. Coupled with thermal energy storage (TES), solar tower plants can operate more than 4500 hours per year at nominal power [1]. Several pressurized air receiver concepts have been proposed and tested with varying levels of success. Since air exhibits a low specific heat capacity compared to other HTFs such as molten salt, higher receiver surface temperatures are required to yield an equivalent power output. This typically constrains pressurized air receivers to cavity configurations to minimize convective and radiative heat losses. Radiative losses may be further reduced by utilizing the volumetric effect [1], whereby the hottest part of the receiver is not directly exposed to the environment. Convective losses are also reduced by covering the receiver aperture, typically through means of a quartz glass window.

Of the proposed pressurized air receiver concepts, only receivers utilizing both the volumetric effect and quartz glass windows have managed to obtain air outlet temperatures over 1000 ˚C [2, 3, 4]. At these high temperatures, receiver materials generally consist of oxide and non-oxide ceramics due to their high melting temperature of around 2000 ˚C. To reduce cost and complexity, recent research has shifted from the volumetric cavity receiver configurations to the development of tubular cavity receivers [5, 6]. The latter is proposed to offer a more robust technology, at the expense of lower air outlet temperatures, typically around 800 ˚C, due to material limitations [7, 8].

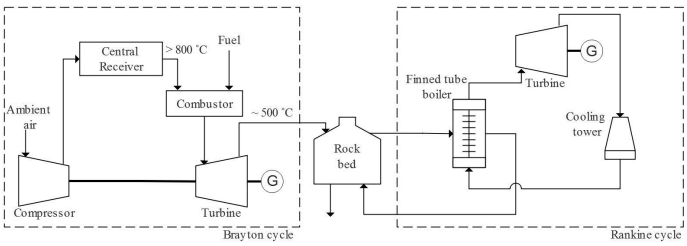

Figure 1: The SUNSPOT cycle [9]

The SUNSPOT [9] cycle (Stellenbosch UNiversity Solar POwer Thermodynamic cycle) shown in Figure 1, is an asynchronous combined Brayton-Rankine cycle that aims to increase thermodynamic efficiency by increasing hot end temperature in the Brayton cycle as well as provide TES in the form of a rock bed for dispatchable power generation at night. Pressurized air from the compressor is heated to above 800 ◦C in the central

receiver (CR). A combustor located upstream of the turbine allows for additional air heating during times of reduced solar radiation, using natural gas or hydrogen as fuel. Exhaust gas at approximately 500 ˚C is ducted from the turbine to a packed rock bed TES facility. At night, hot air from the rock bed is blown through a finned tube boiler, generating steam to drive a bottoming Rankine cycle.

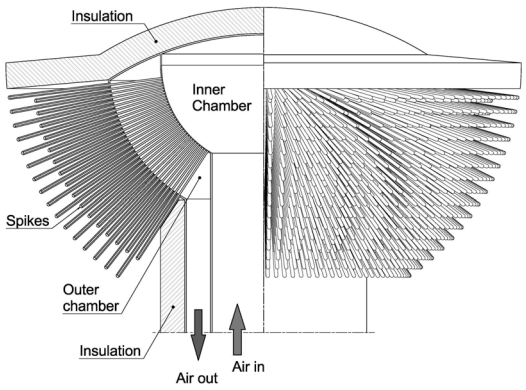

Figure 2: Possible SCRAP layout [11]

The CR technology used in the SUNSPOT cycle to heat incoming air from the compressor would need to provide outlet temperatures of above 800 ˚C, while operating at a low pressure drop to reduce impact on the Brayton cycle efficiency. The Spiky Central Receiver Air Pre-Heater (SCRAP) [10] aims to address the problems faced in current compressed air CR technology. The SCRAP uses "spikes" as tubular absorbers that protrude out from the center of the receiver as shown in Figure 2. The spike consists of two concentric tubes with a finned annulus. Compressed air enters the receiver's inner chamber through the central opening, where it travels through the inner tube of the spike. As the cold air exits the inner tube, it is diverted back through the irradiated outer tube and collected in the outer chamber of the receiver. The spike internal geometry as well as cross section is shown in Figure 3.

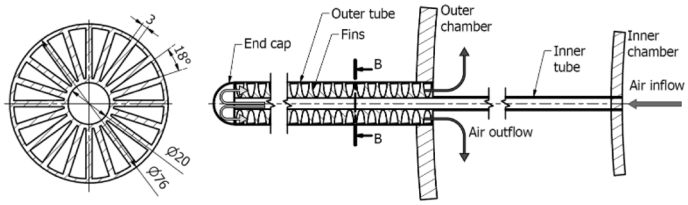

Figure 3: Spike internal geometry [11]

Incoming cold air is preheated by the exiting air and then further heated as it travels back through the outer tube. Solar irradiation on the base, depending on spike positioning, would also serve to heat the air. Due to the jet impingement cooling at the spike tip, the highest spike cooling is expected at the spike tip, which would avoid overheating of the spike section most readily exposed to solar irradiation. The SCRAP receiver has been described as an external semi-volumetric tubular pressurized air receiver. This is because the spikes act as a porous surface, where the highest temperatures are expected at the base of the receiver and not the spike tips. Since the highest temperatures occur within this porous structure with the lowest exposure to the environment, radiation losses are reduced substantially.

In this work, a section of the SCRAP, approximating a full-scale receiver, is constructed, and tested in on-sun conditions. An open annulus spike configuration is initially used to ensure uniform heat transfer rates inside the spike, due to the high cost of implementing a full-length finned spike. A second spike configuration, utilizing a 400 mm coiled fin section at the front of the spike, with the fin geometry shown in Figure 3, is also tested. The coiled fin geometry originates from previous work [12] conducted on the SCRAP, where the intention of the coils is to mitigate the effects of local hot spots caused by uneven circumferential irradiation distribution by allowing the air flow to pass hotter sides of the spike several times. The coils would also enhance internal heat transfer by inducing secondary flow patterns to the air flow.

2. Receiver design and experimental setup

To emulate the view factor between the center spike and the environment and neighboring spikes, and convective shielding, the spike was positioned between two rows of passive spikes. The receiver sizing parameters were derived from a reference design [12] with a sphere radius of 2 m and a spike length of 1 m. With a chosen spike center-to-center distance of 120 mm, the inner and outer spike rows incline at 3˚ and 6 ˚ respectively from the center spike.

The receiver, shown in Figure 4, was installed at Stellenbosch University's Helio40 research facility, shown in Figure 5. The facility houses an 18 m high receiver lattice tower and 12 1.83 m×1.22 m heliostats, of which 10 were functioning reliably for this work. The receiver was aimed at the geometric center of the heliostat field to ensure uniform circumferential irradiation exposure on the spike surface. Previous work [13, 14] conducted at the Helio40 facility with uncooled cavity receiver configurations showed that material temperatures do not exceed 430 ˚C with the current heliostat setup, allowing the receiver to be constructed from mild steel.

Spike wall temperatures were measured at several positions, shown in Figure 6 and Figure 7. Air inlet temperature was measured 200 mm upstream of the receiver inlet. Spike outlet air temperature was measured at the transition from the spike to the air manifold and manifold air temperature was measured 50 mm adjacent to the air inlet. Receiver outlet air temperature was measured at the receiver exhaust outlet, which extends a further

1.5 m from the air outlet. A thermocouple positioned behind the receiver and shaded from direct irradiation was used to measure ambient air and wind temperature at the receiver.

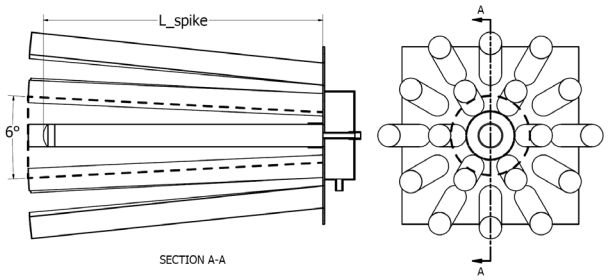

Figure 4: Depiction of as-built geometry and receiver aperture

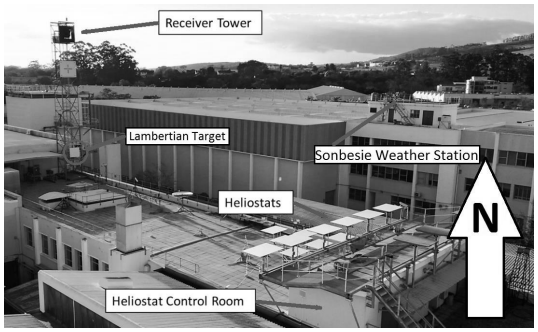

Figure 5: Helio40 layout [14]

Temperature measurements inside the spike fins were taken at 3 circumferential positions. For the finned section closest to the tip, measurements were taken at 0° (top) and 90° (anticlockwise from front). For the rear finned section, measurements were taken at 90˚ and 180˚. Temperature positions and depths are depicted in Figure 7 and Figure 8, where the convention follows T - (1st or 2nd) - (angular position) - (depth). Since the fins are coiled, each temperature position corresponds to a different duct.

Air volumetric flow rate and pressure was measured at the pressurized air feed lines at the bottom of the receiver tower using a Festo SFAM-90 volumetric air flow meter and an Endress+Hauser Deltabar M PMD55 differential pressure transducer. The total air mass flow rate was calculated using the volumetric flow rate and air density, calculated from the ideal gas law. At the time of designing the experimental receiver, suitable pressure sensors or suitable high temperature pressure lines could not be obtained before starting the manufacturing work. The static pressure drop across the spike is therefore not monitored.

DNI was measured using a Kipp & Zonen CMP11 pyranometer positioned at the base of the receiver. The heliostat concentration factor, as a function of the relative angle between the receiver and the sun as viewed from the heliostat, was determined to take the form

$$CF_{avg} = 100.8\Phi^{-1.097} + 4.164 \quad (1)$$

where Φ is determined through the processes outlined by [15] and [16] and given in degrees. The maximum and minimum concentration factors were found to show a consistent variation of 20% from the average concentration factor. Wind speed and direction measurements were obtained from the Sonbesie weather station.

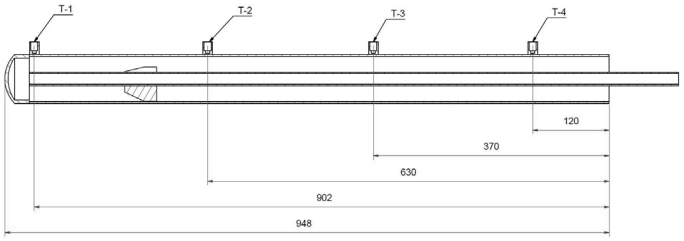

Figure 6: Open annulus spike with thermocouple locations

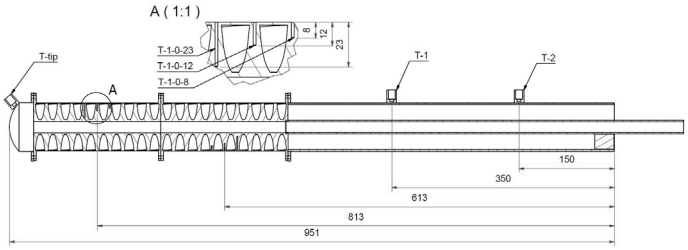

Figure 7: Finned annulus spike with thermocouple locations

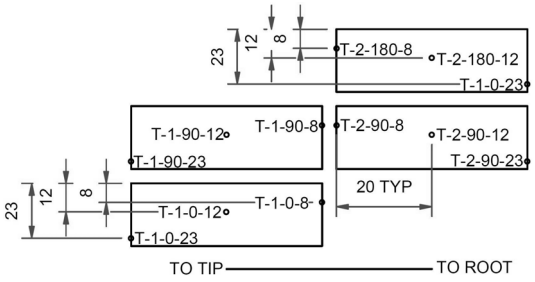

Figure 8: Depiction of fin temperature positions

To calculate the spike's thermal efficiency, the aperture was defined as the total area between the inner spike row as depicted in Figure 4, which is formulated as

$$A_{ap} = \pi\left(L_{spike}\tan 3^\circ + r_{spike} + r_s\right)^2 \quad (2)$$

where r_s is the spike root spacing and r_{spike} is the spike radius of 38 mm. The thermal efficiency is calculated from

$$\eta_{thermal} = \frac{\dot{Q}_{out}}{I_{ap}A_{ap}} \quad (3)$$

where $\dot{Q}_{out}$ is the air energy gain and I_{ap} is the calculated irradiation at the receiver aperture, determined from the measured DNI, heliostat concentration factor and the number of heliostats operating during the tests.

3. Experimental results, analysis, and discussion

Inclement weather dictated that small windows of opportunity were available in which complete data sets could be obtained with favorable weather. The measured data and receiver performance was found to be repeatable, considering the changing weather conditions during individual tests as well as seasonal weather changes during the project. The final tests conducted in favorable weather for each spike configuration are discussed here. For the sake of brevity, only the open annulus spike raw test data is given. The prevailing wind during both tests varied between 200˚-260˚, which was considered predominantly perpendicular to the spike. For this analysis, only the crosswind component is considered where the spike orientation is approximately 210˚.

Due to the relatively low irradiation levels, and subsequent temperatures, attainable with the experimental facility, compared to a full-scale heliostat field, drawing absolute conclusions about a full-scale receiver's performance is problematic. The results do, however, facilitate the assessment of several practical impacts of receiver performance.

Figure 9: Receiver in operation with focal image drift

Due to the relatively small aperture area, the spike was found to be susceptible to heliostat focal image drift as shown in Figure 9. Upon initial calibration, a consistent focal image could be obtained where most of the solar irradiation was concentrated inside the receiver aperture. The combined changing solar angle and heliostat tracking errors caused continual focal image drift and a corresponding performance loss. In a full-scale SCRAP implementation, tracking accuracy and consistency of the heliostat field would be paramount to the thermal performance of the receiver as well as mitigating unwanted thermal cycling in the receiver material, particularly at the spike tip, which is exposed to high irradiation concentrations as well as high jet impingement cooling rates.

3.1. Experimental data

Material and air temperature data for the open annulus spike test are given in Figure 10. Air mass flow rate was increased from a minimum stable flow rate to the maximum obtainable flow rate with the current facilities. Irradiation and wind data are given in Figure 11. Maximum and minimum air outlet temperatures of 67.01 ˚C and 45.2 ˚C were obtained at air mass flow rates of 0.042 kg/s and 0.107 kg/s, respectively. During the test, irradiation on aperture was calculated to range from 51.47 kW/m^2 to 53.44 kW/m^2 with corresponding measured DNI values of 701 kW/m^2 and 917 kW/m^2. Wind speed ranged from 0.86 m/s to 3.78 m/s with wind direction fluctuating between 200˚ - 260˚.

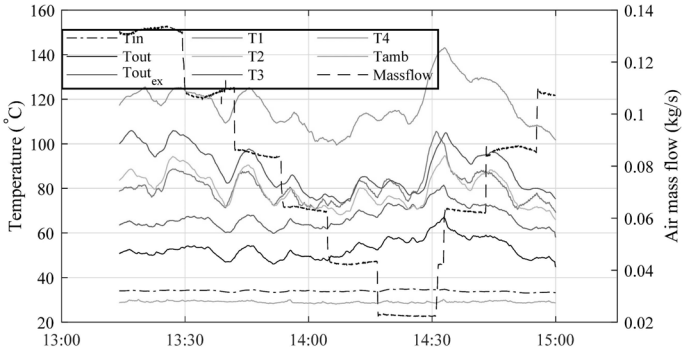

Figure 10: Open annulus temperatures and flow rates

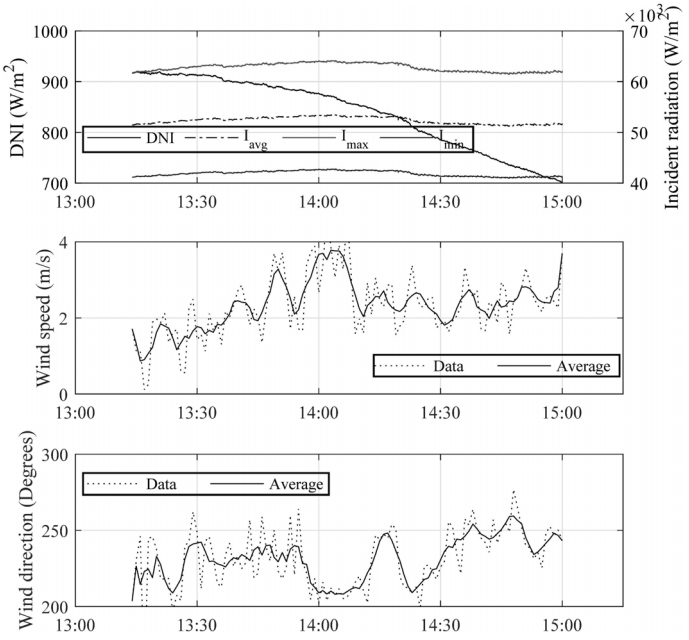

Figure 11: Irradiation and wind data for open annulus spike test

During the test, maximum material temperatures were recorded

at the rear of the spike, with T4 reaching 142.5 ˚C. The front of the spike generally showed lower material temperatures, with the lowest temperature of 68.17 ˚C being recorded at T2. Considering the lowest surface temperature did not occur at T1, behind the tip, this indicates that irradiation concentration towards the front of the spike is relatively low. Here, T1 would be influenced by the tip temperature through axial conduction when the mass flow rate is too low to provide sufficient tip cooling.

3.2. Thermal efficiency

Figure 12 gives the thermal efficiency as a function of air mass flow rate with the 20% concentration factor variation indicated. The open annulus spike exhibited a near-linear efficiency increase from 16% at 0.02 kg/s, to 82% at 0.14 kg/s, with distinct data clusters observed for thermal efficiency at the experienced wind speeds. For the finned annulus spike, a higher low-flow efficiency was observed, increasing non-linearly from 23% at 0.02 kg/s, to 81% at 0.14 kg/s. Both spikes exhibit approximately 80% efficiency at 0.135 kg/s.

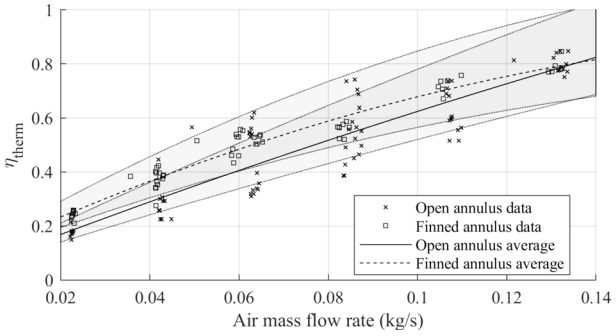

Figure 12: Thermal efficiency with increasing flow rates

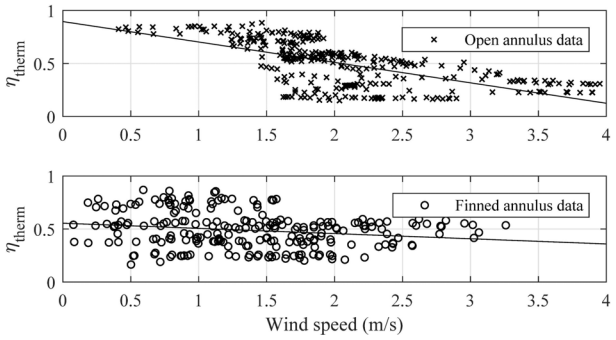

Figure 13: Thermal efficiency with increasing wind speeds

Figure 13 shows the thermal efficiency as a function of crosswind speed with trends represented by least-squares fits. For both spikes, maximum thermal efficiencies of 84% were obtained at low crosswind speeds, suggesting that an asymptotic efficiency has been reached. For both spikes, a similar efficiency reduction was observed with increasing crosswind speed where a maximum thermal efficiency of 30% is observed at crosswind speeds of 3.95 m/s for the open annulus spike.

3.3. Surface temperature and irradiation distribution

Figure 14 gives the open annulus spike surface temperature distribution for increasing air mass flow rates, with the first three positions given as a fraction of T4. Air inlet temperature averaged around 34.5 ˚C. At low flow rates, T1 exhibits higher temperatures than T2, indicating a high degree of axial conduction from the spike tip. This trend continues for flow rates below 0.085 kg/s, where an inflection indicates that a sufficient tip cooling rate has been achieved.

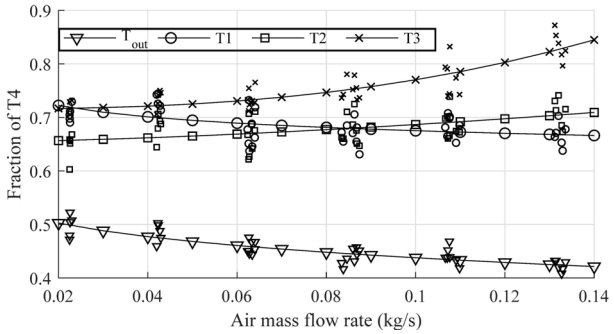

Figure 14: Average open annulus spike surface temperatures

At high mass flow rates, T1 and T2 remain colder than the two rear surface temperatures, T3 and T4, and exhibit a small temperature difference, T2-T1, indicating a lower and more uniform irradiation concentration on the front half of the spike surface. Conversely, the higher temperatures at T3 and T4 indicate higher irradiation concentrations at the rear of the spike. As the receiver base is exposed to direct irradiation, as opposed to oblique irradiation on the spike surface, the base would also reach higher temperatures, contributing to axial heat conduction into the spike.

Due to the general difficulty of explicit irradiation measurement on the spike surface, an axi-symmetric discrete order (DO) irradiation model of the center spike and receiver base as shown in Figure 4, was developed in ANSYS Fluent. The use of the DO method to solve the radiative transfer equation been used successfully in previous work [17, 18] where results comparable to the Implicit Monte Carlo method could be obtained, while permitting the modelling of complex geometries with distinct advantages over readily available ray tracing software packages. The spike and receiver base were modelled as black and grey with ε=0.92 [19], respectively. Stable solutions were obtained with a 4094-cell mesh, using $N_\theta \times N_\Phi = 70 \times 70$ angular divisions and a 2nd-order upwind scheme.

A 1-dimensional heat transfer model incorporating the thermal radiation interaction with the environment and surrounding receiver geometry [20, 19], natural and forced convection losses

[19, 21, 22] and internal forced convection [23] was also developed to investigate the effects of changing irradiation exposure. The model utilizes an explicit formulation with a 1st-order upwind scheme for internal flow elements and a central differencing scheme for the axial conduction interaction between neighbouring wall elements. The 1-D model was verified through CFD modelling of discrete internal flow sections of the open and finned annuli and good agreement was found for the predicted Nusselt numbers. Good agreement was also found for the predicted pressure drops and outlet temperatures.

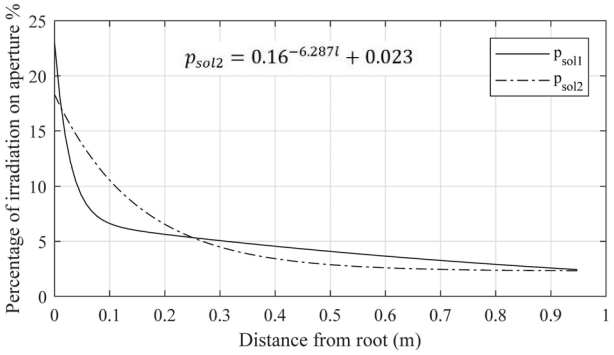

Figure 15: Comparison of irradiation concentration profiles

Two irradiation profiles, p_{sol1} and p_{sol2}, shown in Figure 15, were investigated. p_{sol1} was obtained from the DO irradiation model and p_{sol2} was derived from the surface temperature growth variation in Figure 14, where frontal irradiation is set equal to p_{sol1} and the root irradiation is adjusted so that p_{sol1} and p_{sol2} exhibit the same total irradiation input to the spike surface, within 1%.

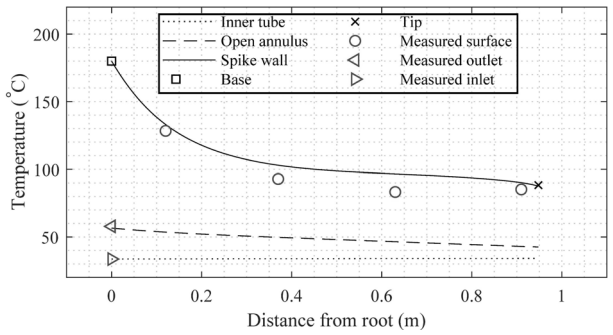

Figure 16: 1-D model output with irradiation profile p_{sol2}

Figure 16 shows an example 1-D model output using p_{sol2} as irradiation input. Quasi-steady state data between 14:38 and 14:42 was used as input data with a flow rate of 0.062 kg/s, irradiation on aperture of 51.49 kW/m^2 and crosswind speed of 1.779 m/s. Maximum surface temperature variations between measured results and the 1-D model were within 10 ◦C for several examples, increasing to within 30 ◦C when p_{sol1} is used as irradiation input, as p_{sol1} produces higher irradiation at the spike root, leading to higher root temperatures and increased axial conduction to the front of the spike. For all samples tested, p_{sol2} provided better approximations of spike wall temperature and, consequently, air outlet temperature leading to the conclusion that p_{sol2} is a reasonable approximation of the real irradiation profile.

From the DO irradiation model, the receiver base experiences 185% of the irradiation on aperture, yielding a root irradiation of 22%. If a linear relationship is assumed, an estimation can be made that the experimental receiver experiences 153% of the irradiation on aperture at the base, giving 18.3% of the irradiation on aperture at the spike root.

3.4. Coiled fin temperature distribution

Figure 17 shows the fin height average temperature profiles for the rear finned section at 180˚ with inlet air temperature fluctuating between 31.01 ˚C and 34.84 ˚C. Centrifugal forces induced by the coiled ducts force the air flow towards the spike wall as air flow develops, leading to high heat transfer coefficients at the wall and adjacent fin section closest to the wall. The highest flow velocities, and subsequent heat transfer coefficients, would occur at the duct centroid, leading to the bulk of the heat transfer from the fin occurring around the centroid. This was observed for the fin geometry used in this work, where the centroid is approximately 10 mm deep as shown in Figure 17, where large temperature gradients were observed between 8 mm and 12 mm. Since most of the heat is removed from the fin close to the spike wall, conduction into the fin is significantly reduced and the remaining fin surface area is underutilised.

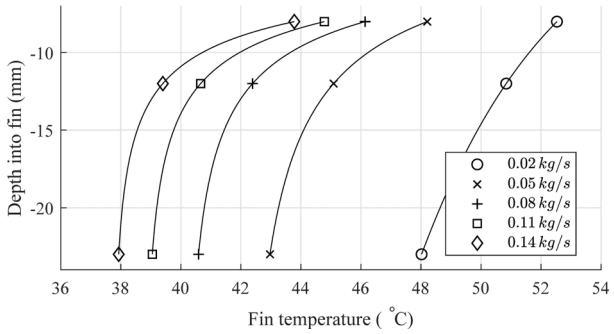

Figure 17: Fin height temperature profiles with increasing flow rates

4. Conclusion

From the experimental results it was found thermal efficiencies of above 80% are obtainable for both spike configurations, however, this was conditional on low wind speeds as the spike was found to be susceptible to convective losses. By replacing the front 40% of the spike with coiled fin sections, an average thermal efficiency increase of 8% was obtained at lower air mass flow rates. The efficiency increase of the finned sections are

diminished at high flow rates where both spikes exhibit the same efficiency at 0.135 kg/s.

In the context of the implementation of a full-scale receiver, the sensitivities to convective losses due to wind and high irradiation concentration at the receiver base poses practical problems. From the presented temperature data, the tip and spike root generally assume the highest temperatures on the spike. When exposed to changes in irradiation exposure, wind speed or wind direction, these components may experience unintended thermal cycling and material fatigue over long term operation.

Initial solutions to mitigating temperature swings at the root and base may include baffles between spikes at different locations on the receiver, resulting in a "honeycomb-like" structure. The inclusion of baffles would also reduce or eliminate convective losses by reducing wind speeds close to the spike root and receiver base. The root and base could be coated with a reflective paint, limiting irradiation absorption. In this scenario, more irradiation would also be reflected to the spike surface.

Of interest is the scalability of manufacturing finned spikes. For the finned sections used in previous work [15], wire cutting was used where manufacturing costs for 314mm of finned section totaled to ZAR 18,639 excluding material cost. For the finned sections used in this work, 3-D printing was used where the total material and manufacturing costs totaled to approximately ZAR 120,000 for 400mm of finned section. These methods are unsuitable for large scale manufacturing and prohibitively expensive for manufacturing the number of spikes required for a full-scale receiver. A possible large-scale alternative may be metal extrusion, conditional on whether the same coiled configurations can be obtained and whether high temperature nickel-base alloys can be used.

At present, the SCRAP struggles to meet the financial and practicality benchmarks, where tubular cavity receivers such as the SOLUGAS [6] would yield comparable levels of thermal performance at a lower financial cost, with the benefit of having been proven to be commercially viable. Objective discussion is therefore warranted by the relevant shareholders of the SCRAP concept to determine its practical and economic feasibility.

Acknowledgements

The financial assistance of the NRF towards this research is hereby acknowledged. Opinions expressed and conclusions arrived at, are those of the author and are not necessarily to be attributed to the NRF.

References

[1] M. Romero, R. Buck and J. Pacheco, "An update on solar central receiver systems, projects, and technologies.," *Journal of Solar Energy Engineering,* vol. 124, no. 2, 2002.

[2] R. Buck , T. Brauning , T. Denk , M. Pfander , P. Schwarzbol and F. Tellez, "Solar-hybrid gas turbine- based power tower systems (refos)," *Journal of solar energy engineering,* vol. 124, no. 1, pp. 2-9, 2002.

[3] A. Kribus, P. Doron, R. Rubin and J. Karni, "A multistage solar receiver: The route to high temperature," *Solar Energy,* vol. 67, no. 1-3, pp. 3-11, 1999.

[4] A. Kribus, P. Doron, R. Rubin, J. Karni, R. Reuven, S. Duchan and E. Taragan, "Performance of the directly-irradiated annular pressurized receiver (diapr) operating at 20 bar and 1,200 degrees," *Journal of solar energy engineering,* vol. 123, no. 1, 2001.

[5] L. Amsbeck, R. Buck , P. Heller , J. Jedamski, R. Uhlig and L. Amsbeck , "Development of a tube receiver for a solar-hybrid microturbine system," in *14th SolarPACES Conference*, Las Vegas, 2008.

[6] R. Korzynietz, J. Brioso, A. del RÃo, M. Quero , M. Gallas, R. Uhlig, M. Ebert, R. Buck and D. Teraji, "Solugas - a comprehensive analysis of the solar hybrid brayton plant," *Solar energy,* no. 135, pp. 578-589, 2016.

[7] A. L. Avila-Marin, "Volumetric receivers in solar thermal power plants with central receiver technology," *Solar energy,* vol. 85, no. 5, pp. 891-910, 2011.

[8] K. Freudenstein and B. Karnowsky, Volumetric ceramic receiver cooled by open air flow-feasibility study, Springer, 1987.

[9] D. Kröger, "Sunspot - the stellenbosch university solar power thermodynamic cycle. Tech. Rep.," Stellenbosch University, 2012.

[10] D. Kröger, "Spiky central receiver air pre-heater (scrap). Tech. Rep.," Stellenbosch University, 2008.

[11] M. Lubkoll, T. von Backström, T. Harms and D. Kröger, "Initial analysis on the novel spiky central receiver air pre-heater (scrap) pressurized air receiver," *Energy Procedia,* vol. 69, pp. 461-470, 2015.

[12] M. Lubkoll, "Performance characteristics of a spiky central receiver air pre-heater (SCRAP)," Stellenbosch University, 2017.

[13] E. J. J. Basson , "Development and testing of an externally finned tube cavity receiver for Brayton cycle preheating purposes," Stellenbosch University, 2019.

[14] H. Joubert, "Development of a Web-based Control System for a Heliostat Test Facility," Stellenbosch University, 2019.

[15] J. Duffie and W. Beckman, Solar engineering of thermal processes. 3rd edn., Wiley, 2006.

[16] W. Stine and M. Geyer, Power from the Sun, 2001.

[17] K. Craig, J. Meyer and W. Le Roux, "Computational fluid dynamics analysis of parabolic dish tubular cavity receiver," in *3rd Southern African Solar Energy Conference*, South Africa, 2015.

[18] M. Moghimi, K. Craig and J. P. Meyer, "A novel computational approach to the combine optical and thermal modelling of a linear fresnel collector receiver," in *3rd Southern African Solar Energy Conference*, 2015.

[19] Y. Çengel and A. Ghajar, Heat and mass transfer: fundamentals and applications, McGraw-Hill Higher Education, 2015.

[20] J. Howell , A catalog of radiation configuration factors., McGraw-Hill, 1982.

[21] S. Whitaker, "Forced convection heat transfer correlations for flow in pipes, past flat plates, single cylinders, single spheres, and for flow in packed beds and tube bundles," *AIChE Journal,* vol. 18, no. 2, p. 361–371, 1972.

[22] A. Žukauskas, "Heat transfer from tubes in crossflow," *Advances in heat transfer,* vol. 8, pp. 93-160, 1972.

[23] J. Dirker and J. Meyer, "Convection heat transfer in concentric annuli," *Experimental heat transfer,* vol. 17, no. 1, pp. 19-29, 2004.